# Al 1*s*–2*p* Absorption Spectroscopy of Shock-Wave Heating and Compression in Laser-Driven Planar Foil

## Introduction

A physical understanding of the shock-wave heating, radiative heating, and heating by energetic electrons in direct-drive inertial confinement fusion (ICF) is required to control the pressure in the main fuel layer.[1] A direct-drive hot-spot ignition ICF target consists of a spherical cryogenic fuel shell of deuterium and tritium surrounded by a thin plastic layer.[2] It is illuminated by symmetrically arranged intense laser beams having a temporal laser shape of a low-intensity foot followed by the gradual increase to a high-intensity main drive. The foot intensity launches a weak shock into the target, and the ramp of the laser intensity launches multiple shock waves with increasing strengths (compression wave) to isentropically compress the shell and implode the target to form a central hot spot with sufficient fuel areal density and temperature for ignition. The shell entropy or adiabat ($\alpha$), defined as the ratio of the pressure in the fuel layer to the Fermi pressure, relates to the ICF target performance and the stabilization of Rayleigh–Taylor (RT) hydrodynamic instabilities.[3] The minimum energy required for ignition scales to $E_{\text{ig}} \sim \alpha^{1.88}$, while the ablation velocity that stabilizes the RT growth is proportional to $V_a \sim \alpha^{3/5}$ (Ref. 3). Therefore, a successful direct-drive ICF implosion design with energy gain creates an adiabat in the shell that strikes a balance between the laser-energy requirement and the target stability.

The shock wave launched by laser ablation is the dominant heating mechanism that sets the shell adiabat. After a coronal plasma is formed, the ablation process is driven by the energy flow via electron thermal transport from the critical density and the ablation surface (conduction zone). The incident laser can propagate into the plasma up to the critical density where the laser frequency is equal to the plasma frequency $\left(n_{\text{c}} = 1.1 \times 10^{21}/\lambda_{\mu\text{m}}^2\right)$. The laser energy that is absorbed near the critical-density surface is thermally transported by electrons to the ablation surface where the outer surface of the target is ablated and a shock wave is launched inward. The shell accelerates via the rocket effect. Modeling of electron thermal transport in the conduction zone is challenging because the steep temperature gradient in the plasma causes the classical Spitzer–Härm thermal conductivity[4] to break down. The 1-D hydrodynamics code *LILAC*[5] uses a flux-limited thermal transport model[6] to calculate the heat flux. It takes the minimum value of the heat flux calculated with either the classical Spitzer–Härm thermal conductivity ($q_{\text{SH}} = \kappa \nabla T_{\text{e}}$, where $\kappa$ is the Spitzer conductivity)[4] or an artificially inhibited, free-streaming heat flux ($q_{\text{FS}} = n_{\text{e}} T_{\text{e}} v_{\text{th}}$, where $v_{\text{th}}$ is the thermal electron velocity) [i.e., $q = \min\left(q_{\text{SH}}, f \bullet q_{\text{FS}}\right)$, where $f$ is the empirically determined flux limiter]. The typical value of $f$ for simulations of direct-drive experiments is $0.04 < f < 0.1$. Although simulations with a constant flux limiter and experiments agree well, simulations with the same value of $f$ do not consistently match to the all experimental data.[7] For instance, shock-velocity measurements in CH foils on OMEGA[8] agree with the simulation with $f = 0.06$, while the Richtmyer–Meshkov-growth measurements are in agreement with $f = 0.1$ (Ref. 9). A nonlocal electron-transport model developed by Goncharov[10] has shown consistent agreement between these two experiments and the simulations.[9] The nonlocal model acts like a time-dependent flux limiter and includes the transport of high-energy electrons in the tail of the electron-velocity distribution. X-ray radiation from the corona and suprathermal (energetic) electrons generated from two-plasmon-decay (TPD) instability[11] have been identified as possible target-heating sources.[12] These mechanisms could preheat the target before the shock-wave heating occurs. This preheating could increase the shell adiabat, reduce the compressibility of the fuel, and lead to a degradation of the ICF target performance.

The plasma conditions of a direct-drive, shock-wave–heated, compressed target are predicted to be in a warm-dense-matter (WDM)[13] regime where the degree of degeneracy and the electron–electron coupling parameter[14] are of the order of unity and the ion–ion coupling parameter exceeds 1 (Ref. 15). The electron–electron coupling parameter $\Gamma_{\text{ee}}$ is defined as the ratio of Coulomb potential between free electrons to the average kinetic energy of the free electrons [$\Gamma_{\text{ee}} = e^2/dk_{\text{B}}T_{\text{e}}$, where $d = (3/4\pi n_{\text{e}})^{1/3}$ is the average interparticle spacing]. The degree of degeneracy $\Theta$ is the ratio of the Fermi temperature to the electron temperature $\left(\Theta = T_{\text{F}}/T_{\text{e}}\right)$. Diagnostic techniques to probe plasma conditions in the WDM regime are limited because the electron temperature of the plasma is too low for it to emit x rays and its density (above solid density) is too high to be probed with optical lasers for Thomson-scattering measurements.[16] These extreme conditions have been diagnosed with x-ray scattering[17,18] and x-ray absorption spectroscopy.[19,20] Spectrally resolved x-ray scattering has been demonstrated to probe these plasmas created with radiative heating[17,21] and direct-drive, shock-wave heating.[22] Scattering experiments require a relatively large amount of matter to scatter a sufficient number of incident x rays, limiting its spatial resolution. Although it requires a buried mid-$Z$ tracer layer in the shock-wave–heated foil, x-ray absorption spectroscopy measurements can provide time-resolved local measurements. The temporal and spatial resolution of the time-resolved x-ray absorption spectroscopy is sufficient to resolve the shock-wave heating from heat-front penetration.

Local plasma conditions during shock-wave heating and compression, as well as the timing of heat-front penetration, are diagnosed with time-resolved Al 1$s$–2$p$ absorption spectroscopy of planar plastic foils with a buried tracer layer of Al. Plastic foils are surrogates for cryogenic fuel layers. The objective of this article is to test electron-thermal-transport models in *LILAC* by comparing the predicted shock-wave–heated plasma conditions with measurements and to determine if additional heating due to energetic electrons or x-ray radiation from the coronal plasma is significant. The CH/Al/CH drive foil was directly irradiated with peak intensities of $10^{14}$ to $10^{15}$ W/cm$^2$ and probed with a point source of Sm backlighter irradiated with laser intensities of ~$10^{16}$ W/cm$^2$ (Ref. 19). The measured Al 1$s$–2$p$ spectra were analyzed with the atomic physics code *PrismSPECT*[23] to infer $T_e$ and $\rho$ in the buried Al layer, assuming uniform plasma conditions during the shock-wave heating and compression, and to determine when the heat front penetrated the Al layer. Strong shock waves and isentropic compression were studied. This is the first observation of plasma conditions created with a compression wave.[24] The level of shock-wave heating and timing of heat-front penetration inferred from the experiments were compared with the post-processed *LILAC* simulations using the time-dependent atomic physics code *Spect3D*.[25] The shock-wave heating and heat-front penetration predicted by *LILAC* using $f = 0.06$ or the nonlocal model agree with experimental results for times when the shock is transiting the foil. At late times in the drive, observed discrepancies between the predicted and measured plasma conditions in the Al layer are attributed to reduced radiative heating due to lateral heat flow in the corona. Therefore, preheat due to energetic electrons near the end of the laser drive could not be resolved in this experiment.

The following sections of this article (1) describe the setup of the x-ray absorption spectroscopy experiment on OMEGA; (2) present 1-D *LILAC* simulations and absorption spectra calculated from the post-processed *LILAC* using *Spect3D*; (3) present measured streak spectra and analyses of Al 1$s$–2$p$ absorption spectra with *PrismSPECT*; (4) discuss and present results for square and shaped laser drives; (5) briefly mention future work; and (6) summarize results.

## Experiment

The experiment consists of three main components: a point-source Sm backlighter, a CH/Al/CH drive foil, and a Bragg crystal spectrometer, with a schematic (not drawn to scale) shown in Fig. 116.23. The relative alignment of these three components is crucial for the success of the experiment. A 50-$\mu$m planar CH foil with a 1- or 2-$\mu$m buried Al layer was irradiated with up to 21 OMEGA laser beams[8] that were smoothed with distributed phase plates (DPP's),[26] 1-THz, 2-D smoothing by spectral dispersion (SSD),[27] and polarization smoothing (PS).[28] The overlapped intensity was uniform

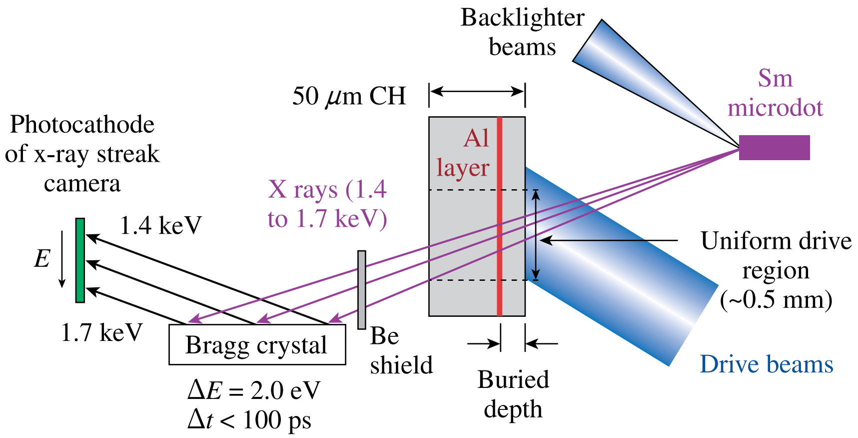

Figure 116.23
A schematic of the Al 1$s$–2$p$ absorption spectroscopy experiment showing a point-source Sm backlighter, a plastic drive foil with a buried Al layer, a Be blast shield, and a Bragg crystal spectrometer coupled to an x-ray streak camera.

over a 0.5-mm-diam spot and peak intensities in the range of $10^{14}$ to $10^{15}$ W/cm$^2$. The overall thickness of the drive foil was chosen based on competing considerations of hydrodynamic instabilities and transmission of the target to ~1.5-keV x rays. Hydrodynamic instabilities due to target acceleration could compromise the spatial resolution of the measurement by mixing the Al layer with the CH.[29] Since the acceleration phase is delayed as the target thickness is increased, thicker targets are less susceptible to hydrodynamic instabilities than thinner ones; however, thicker targets attenuate the x-ray backlighter more than thinner ones. Choosing a drive foil with a 50-$\mu$m thickness was a good compromise. The buried depth of the layer was varied to probe the plasma conditions in different regions of the target. Al 1*s*–2*p* absorption spectroscopy of the drive foil was performed with a point-source Sm microdot backlighter irradiated with six tightly focused (~100-$\mu$m spot) laser beams having an overlapped intensity of ~$10^{16}$ W/cm$^2$. This creates the well-defined Bragg reflection geometry necessary for this experiment. Source broadening can degrade the spectral resolution of the measurement. In contrast to the point-source Sm backlighter, the CH coronal plasma of the drive foil having an ~1-mm diameter does not create a well-defined Bragg reflection geometry. The coronal plasma emission contributes a background signal that degrades the contrast of the absorption features. The size of the Sm backlighter source was monitored with an x-ray framing camera and found to be less than 100 $\mu$m. The Sm M-shell emission provided a relatively smooth continuous spectrum in the 1.4- to 1.7-keV range, which overlaps the Al 1*s*–2*p* absorption features around 1.5 keV and probes the uniformly driven portion of the target (see Fig. 116.23).[20] The transmitted spectrum was recorded with an x-ray streak camera[30] outfitted with a Bragg crystal spectrometer that used a flat RbAP crystal[31] to disperse the spectrum onto a low-density (fluffy) CsI photocathode.[32] Each of the three components was positioned independently to ensure that the driven portion of the target was being probed with the Al 1*s*–2*p* absorption spectroscopy. Since alignment of the experiment was based on mechanical references, it was extremely reproducible. In a contrast measurement calibration using a Pb slit plate on the x-ray photocathode of the streaked x-ray spectrometer, a spectral resolution of 2.0 eV ($E/\mathrm{d}E \sim 750$) was estimated from the sharpness of the measured step function.[33] The dynamic range of the x-ray streak camera was measured to be ~50. The relative time axis of the x-ray streak spectra was established using the UV timing fiducial on OMEGA. The x-ray streak camera has a uniform streak speed with an average speed of 115 ps/mm.[34] It uses a microchannel-plate (MCP)[35] image intensifier, and the streaked spectrum is recorded on Kodak TMAX 3200 film. The film is converted from optical density to a linear intensity scale using the step wedge imprinted on each roll of film. The frequency-dependent transmission of a shocked Al layer was obtained from the ratio of transmitted Sm spectra through CH drive foils with and without an Al tracer layer.

### One-Dimensional Simulations

Direct-drive plastic foils with a buried Al tracer layer were simulated with the 1-D hydrodynamics code *LILAC*[5] using either a flux-limited[6] or a nonlocal thermal transport model.[10] A flux-limited transport model calculates heat flux with either the classical Spitzer thermal conduction ($q_{\mathrm{SH}} = \kappa \nabla T_{\mathrm{e}}$) or a fraction of free-streaming flux ($q_{\mathrm{FS}} = n_{\mathrm{e}} T_{\mathrm{e}} v_{\mathrm{th}}$). The Spitzer transport model is valid only when the mean free path of electrons ($\lambda_{\mathrm{e}}$) is much shorter than the electron-temperature scale length $\left[L_T = T_{\mathrm{e}} \big/ \left(\mathrm{d}T_{\mathrm{e}} \big/ \mathrm{d}x\right)\right]$. When $\lambda_{\mathrm{e}}$ is comparable to $L_T$ such as in a conduction zone with a steep temperature gradient, a flux-limited free-streaming flux ($q = f \bullet q_{\mathrm{FS}}$) is used to model the heat flux. The flux limiter was either 0.06 (lower heat flux) or 0.1 (higher heat flux) in these simulations. A higher flux limiter in the model allows more energy to flow from the critical density to the ablation surface, producing a stronger shock wave compared to a flux limiter with a lower value. A nonlocal model developed by Goncharov[10] does not require a flux limiter to calculate heat flux. It solves a simplified Boltzmann equation using the Krook collision model and calculates heat flux using a convolution with the Spitzer heat flux and a delocalization kernel. This nonlocal treatment of the thermal transport includes time dependence of a reduced heat flux from the Spitzer model in plasmas with a steep temperature gradient and nonlocal preheat due to long-range electrons from the coronal plasma. Details of the nonlocal electron-transport model are described in Refs. 10 and 36. The radiation transport is modeled in *LILAC* with multigroup diffusion using the Los Alamos National Laboratory astrophysical tables[37] for the opacities. The equation of state (EOS) is modeled using the *SESAME* tables[38] for both CH and Al. The serial numbers of *SESAME* EOS used in *LILAC* for these experiments are 7593 for CH and 3720 for Al.

Figure 116.24 shows the 1-D spatial profiles of the electron temperature and mass density predicted by *LILAC* in a drive foil during shock-wave heating and heat-front penetration using a flux limiter of 0.06. As the shock wave launched by laser ablation propagates through the Al layer, it compresses the layer and creates uniform plasma conditions in the target behind the shock wave [Fig. 116.24(a)]. The predicted electron temperatures due to shock-wave heating in the experiment are in the range of 10 eV to 40 eV. The uniform plasma approximation is valid until the ablation surface reaches the Al. Once the heat front penetrates into the Al layer, it creates strong gradients of $T_e$ and $\rho$ as shown in Fig. 116.24(b). The *LILAC* predictions are post-processed with *Spect3D*[25] to simulate the Al 1*s*–2*p* absorption spectral line shapes. Both *Spect3D* and the atomic physics code *PrismSPECT*[23] use level populations of detailed configuration accounting (DCA) to compute absorption spectra. The Stark-broadened line shapes are calculated using the Multi-Electron Radiator Line Shape (MERL) code.[39] MERL uses the adjustable parameter exponential approximation (APEX)[40] for ion microfield calculation and a quantum-mechanical relaxation approximation for electron broadening.[41] Figures 116.24(c) and 116.24(d) show Al absorption spectra post-processed *LILAC* profiles of uniform conditions and strong gradients shown in Figs. 116.24(a) and 116.24(b). The spatial profiles of the electron temperature and density from *LILAC* simulations are taken into account in calculating the Al absorption spectra. As shown in Fig. 116.24(c), a few absorption features (F-like, O-like, and N-like features) are created in the uniform condition, while the strong $T_e$ gradient in the Al creates a wide range of 1*s*–2*p* absorption features from F-like to Li-like in Fig. 116.24(d). Both synthetic and measured absorption spectra were analyzed with *PrismSPECT* to infer $T_e$ and $\rho$ during the shock-wave heating and to establish a range of upper and lower limits of $T_e$ during heat-front penetration, as described in the next section.

## Analysis of Measured Absorption Spectra

Figure 116.25 shows examples of the x-ray streak images recorded from CH targets (a) with and (b) without an Al layer (shot 48232 and 48233, respectively). The drive and backlighter beams were co-timed at $t = 0$ ns. The drive foil was irradiated with a shaped laser pulse having a foot intensity of $3 \times 10^{14}$ W/cm$^2$ and a peak intensity of $8 \times 10^{14}$ W/cm$^2$. The time

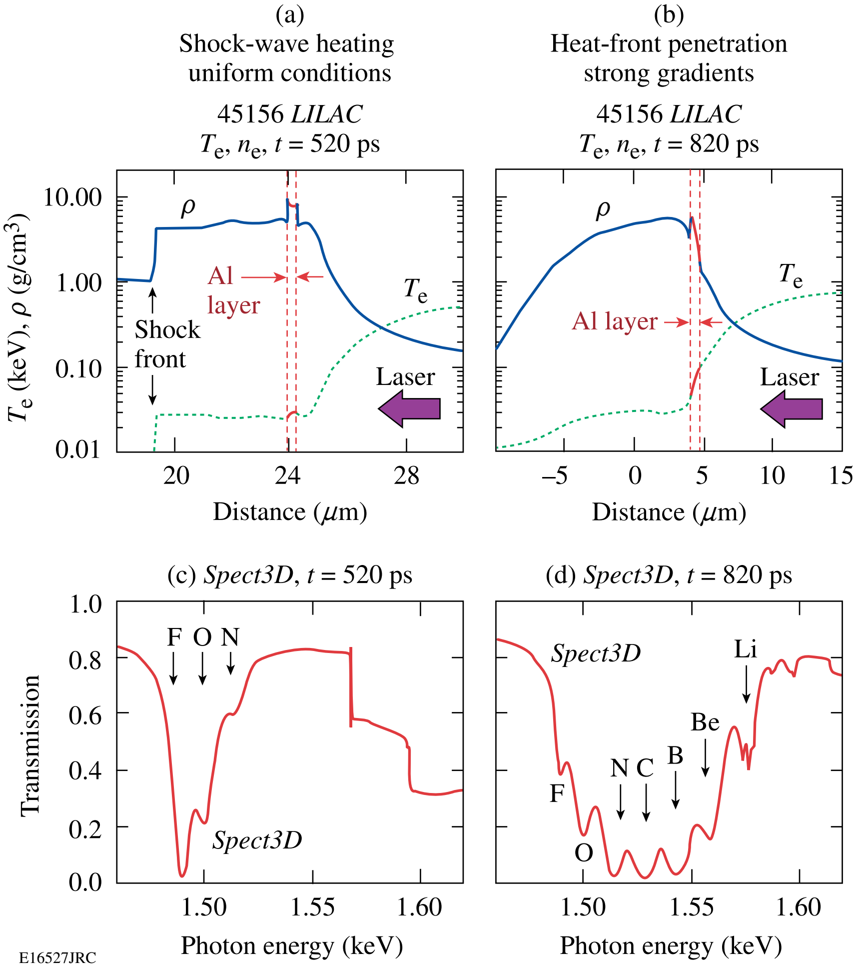

Figure 116.24
Simulated spatial profiles of electron temperature (dotted) and mass density (solid) during (a) shock-wave heating and (b) heat-front penetration. The Al absorption spectra simulated by post-processing *LILAC* with *Spect3D* are shown in (c) and (d). The prominent Al 1*s*–2*p* absorption features are identified.

axis of the streak images was established based on the average measured sweep speed (115 ps/mm) of the x-ray streak camera. The time $t = 0$ ns represents the time on the rising edge of the x-ray intensity when each measured streak reached 2% of the peak intensity. The absolute timing of the measured x-ray streak was established by synchronizing the measured onset of shock-wave heating in the buried Al layer with that predicted by the *LILAC* simulation. The experimental signature of shock-wave heating in the Al layer is a shift in the photon energy of the Al K edge at 1.56 keV. If the electron temperature is above ~10 eV, the shifting K edge is accompanied by the appearance of the F-like Al 1*s*–2*p* absorption. In this experiment, the shifting K edge was used as a timing fiducial in the measured spectra for synchronization with the *LILAC* simulations. The difference in shock timings predicted by *LILAC* using $f = 0.06$ and $f = 0.1$ is less than the experimental temporal resolution of 60 ps. A good timing fiducial around $t = 0$ in the x-ray streak does not exist for most of the drive conditions studied because the initial x-ray emission from the coronal plasma of the drive foil is usually below detection threshold of the streaked x-ray spectrometer. The spectral dispersion for the streak data was calibrated using the K-shell emission from a point-source Mg backlighter. Shortly after the laser irradiates the drive foil, the shock heats and compresses the buried Al layer. As shown in Fig. 116.25(a), the experimental signature of the shock-wave heating is the appearance of the Al 1*s*–2*p*, F-like absorption feature and a blue shift in the Al K edge. When the heat front penetrates the Al layer, a wide range of the higher charge states up to the Be-like feature appears as seen after 1.0 ns. None of these features appear in Fig. 116.25(b) since the CH drive foil does not have an Al layer. The streak images were temporally binned and averaged over a temporal resolution of 60 ps. The apparent absorption-like feature observed at 1.58 keV is an artifact caused by a portion of the photocathode with low sensitivity for this particular shot.

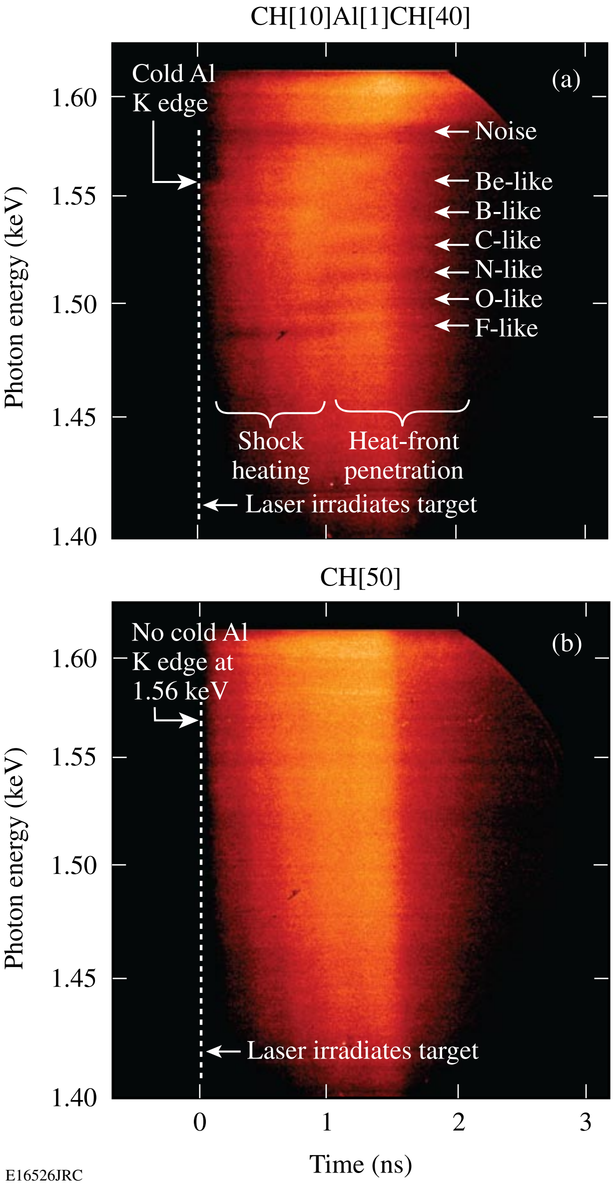

Figure 116.25
Measured streak images from (a) a CH foil with a buried Al layer and (b) a pure CH foil driven by the $\alpha = 3$ drive with a peak intensity of $8 \times 10^{14}$ W/cm$^2$.

An *in-situ* calibration of the x-ray streak spectrometer was performed to eliminate contamination of background light from the measured intensity signals. An examination of the measured cold Al K edge at 1.56 keV from an undriven CH/Al/CH foil showed a degradation in contrast compared to the modeled contrast of the cold Al K edge.[42] Since there is no coronal plasma emission from the undriven target and the dynamic range of the detector (~50) does not limit the measured contrast, the cause of the degraded contrast was attributed to secondary fluorescence that occurs when intense x rays interact with a Bragg crystal or device parts of the spectrometer.[43,44] The fluorescence level was assumed to be proportional to a fraction of peak x-ray intensity and to contribute a constant background across the x-ray photocathode. This background light must be subtracted from the measured signals to calculate the transmission of the CH/Al/CH drive foil. There are two sources of background light for a driven target shot: x-ray fluorescence of the Bragg crystal and x-ray emission from the coronal plasma of the drive foil. For a driven target shot, the level of background was estimated prior to the shock arrival at the buried Al layer based on corrections of the measured contrast at the K edge. After the shock propagated through the Al layer, the total background level from the coronal plasma and x-ray fluorescence was estimated based on comparisons of measured Al 1*s*–2*p* absorption to *LILAC*/*Spect3D* predictions. A constant background was subtracted for both the absorption and the incident spectra.

The measured spectra with background corrections were fit with *PrismSPECT*[23] assuming uniform conditions for various combinations of $T_e$ and $\rho$. *PrismSPECT* is a nonlocal-thermodynamic-equilibrium (NLTE), collisional-radiative code that calculates the absorption spectrum assuming a uniform slab plasma for a given $T_e$, $\rho$, and $\Delta L$. The product of $\rho$ and $\Delta L$ (areal density) for an Al layer is assumed to be conserved throughout the planar experiment. Figure 116.26 shows measured spectra fit with *PrismSPECT* at (a) $t = 360$ ps during shock-wave heating and (b) $t = 1224$ ps during heat-front penetration for shot 48232 shown in Fig. 116.25. The best fit to the measured spectra during shock-wave heating was determined based on a least-squares-fitting routine, which inferred $T_e$ and $\rho$ simultaneously. The plasma condition inferred from the fit in Fig. 116.26(a) is 22 eV (±2 eV) and 6 g/cm$^3$ (±3 g/cm$^3$). The ionization caused by shock-wave heating and compression can be obtained with different combinations of electron temperature and density; therefore, the inference of electron temperature is limited by the uncertainty in compressed density. The error estimates from the spectral-fitting routine were determined by doubling the minimum $\chi$-squared value.[45] The uncertainty of the inference of $T_e$ due to background subtraction has been considered by varying the estimated background levels for the drive intensity of $1 \times 10^{14}$ W/cm$^2$ (Ref. 33). The uncertainties in the $T_e$ and $\rho$ inferences in this experiment were estimated to be ~10% and ~20% to 50%, respectively.

The experimental signature of heat-front penetration is the onset of absorption from a wide range of higher charge states of Al. The measured spectra at the time of the heat-front penetration were qualitatively compared to the product of two calculated spectra as shown in Fig. 116.26(b). Because of the strong gradients in $T_e$ and $\rho$ when heat front penetrates, the absorption spectrum cannot be fit by a calculated spectrum with a single $T_e$ and $\rho$. Spatially resolved measurements of electron-temperature and density profiles in the conduction zone are challenging. To identify the time of heat-front penetration, it was assumed that the Al layer has two regions that determine a range of the plasma conditions: (1) a lower-density and higher-temperature region characteristic of matter ablated into the conduction zone, and (2) a higher-density and lower-temperature region characteristic of the shock-heated and compressed matter. The inferred ranges of $T_e$ and $\rho$ from the measured spectrum shown in Fig. 116.26(b) are 47 eV < $T_e$ < 70 eV and 2.5 g/cm$^3$ < $\rho$ < 3.5 g/cm$^3$. The initial areal density ($\rho\Delta L$) was equally divided into two parts. The total spectrum is a product of the calculated transmission spectra from each region and can be compared with the overall shape of measured spectra to roughly deter-

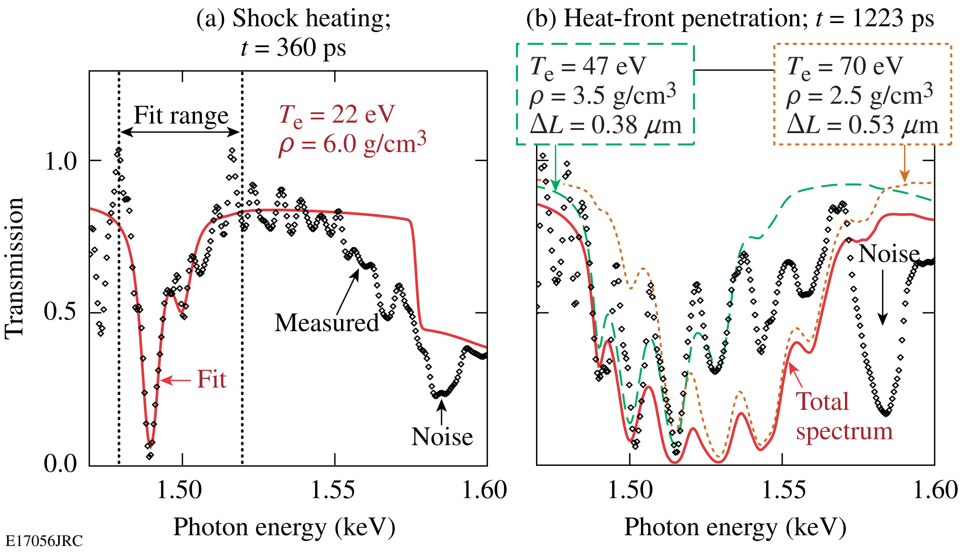

Figure 116.26
(a) A measured spectrum during shock-wave heating (diamond) and fit (thick black curve) obtained in a least-squares-fitting routine to infer $T_e$ of 22 eV and $\rho$ of 6.0 g/cm$^3$. (b) A measured spectrum during heat-front penetration and spectral analysis using two calculated spectra to determine upper and lower limits of $T_e$ for shot 48232. The modeled spectra are calculated with $T_e = 47$ eV and $\rho = 3.5$ g/cm$^3$ for the lower limit (thin dashed black curve) and $T_e = 70$ eV and $\rho = 2.5$ g/cm$^3$ for the upper limit (thin dotted black curve). The total modeled spectrum (thick solid black curve) is obtained by the product of the two spectra.

mine the upper and lower limits of $T_e$. Although this is not a quantitative fitting, the procedure satisfies the experimental objective to identify the time of heat-front penetration by finding when a wide range of temperatures (greater than the shock-heated temperature) exists in the Al layer.

## Results and Discussion

Time-resolved electron temperatures inferred from the experiments during shock-wave heating and heat-front penetration were compared with post-processed *LILAC* simulations using a nonlocal thermal-transport model,[10] as well as flux-limited models[5] with $f = 0.06$ and $f = 0.1$. The laser pulse shapes used in the experiment—1 ns square ($1 \times 10^{15}$ W/cm$^2$ and $4 \times 10^{14}$ W/cm$^2$), 3 ns square ($1 \times 10^{14}$ W/cm$^2$), $\alpha = 3$ (peak intensities of $8 \times 10^{14}$ W/cm$^2$ and $1 \times 10^{15}$ W/cm$^2$), and $\alpha = 2$ pulses—are shown in Fig. 116.27. The target adiabat in this experiment is predicted to be $1.5 < \alpha < 5$. Square laser pulses launch a single shock wave through a CH/Al/CH foil, and a shell adiabat of 5 is created by the 1-ns square pulse with a peak intensity of $1 \times 10^{15}$ W/cm$^2$. A shaped laser pulse drive with a low-intensity foot pulse that gradually increases to a constant high-intensity main drive produces a lower adiabat in the target. The adiabat of a CH/Al/CH foil driven with a shaped pulse is set by the foot intensity. The slowly rising intensity of the main drive produces a series of hydrodynamic waves as the drive pressure slowly increases (i.e., a compression wave). Ideally, isentropic target compression is achieved with a shaped laser pulse. The observation of plasma conditions created with a weak shock and a compression wave in direct-drive planar targets is presented in this section. The laser pulse shape and the number of drive beams were selected to achieve a desired target adiabat $\alpha$ and peak intensity. The buried depth of the Al tracer layer was varied to probe different portions of the target.

### 1. Plasma Conditions Achieved with Square Laser Pulses

Peak laser intensities of $1 \times 10^{14}$ W/cm$^2$, $4 \times 10^{14}$ W/cm$^2$, and $1 \times 10^{15}$ W/cm$^2$ were generated for the square laser pulses using either a 1-ns or 3-ns square laser pulse shape. *LILAC* predicted that the pressures of the single shock wave launched by these drive intensities were 15, 40, and 70 Mbar, respectively. The Sm backlighter target was irradiated with the same pulse shape as the CH/Al/CH drive foil. The absorption spectra recorded just after shock-wave heating are compared with the fitted line shapes in Fig. 116.28. The Al layer was buried at 10 $\mu$m for each of these shots. The lowest-intensity shot had an Al thickness of 2 $\mu$m and the other shots had an Al thickness of 1 $\mu$m. This improved the signal-to-noise ratio of the absorption spectra recorded with the lowest-intensity drive. As drive intensity is increased, the shock-wave pressure increases and higher Al charge states are observed in 1*s*–2*p* absorption. Only the F-like charge state was recorded for the lowest drive intensity ($1 \times 10^{14}$ W/cm$^2$), while F-like, O-like, N-like, and C-like charge states are observed for

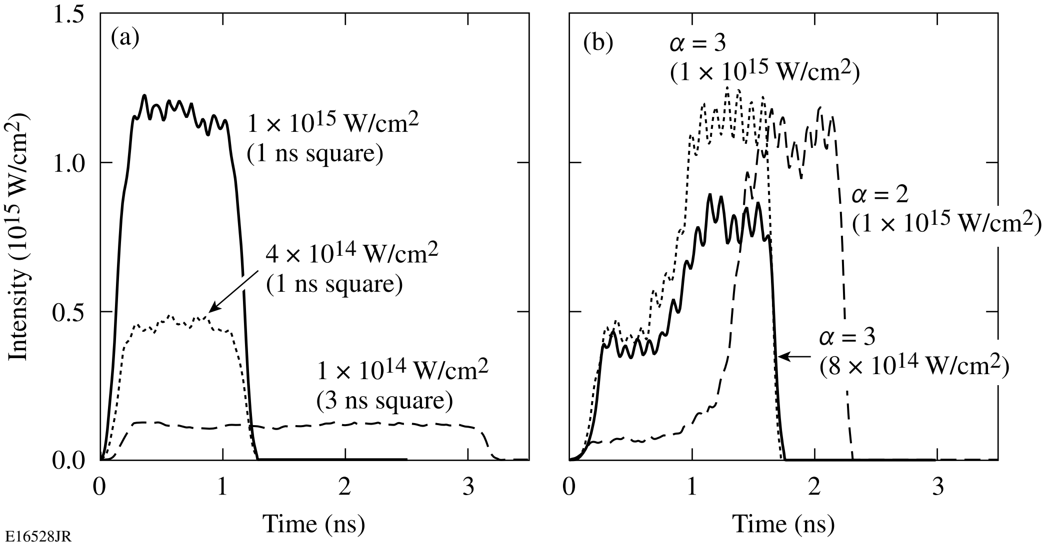

Figure 116.27
Laser pulse shapes for (a) square pulse shapes (1 ns square and 3 ns square) and (b) shaped pulse shapes ($\alpha = 3$ and $\alpha = 2$). The peak intensities for the square laser pulses are $1 \times 10^{14}$ W/cm$^2$ (dashed), $4 \times 10^{14}$ W/cm$^2$ (dotted), and $1 \times 10^{15}$ W/cm$^2$ (solid). For the $\alpha = 3$ drives, the peak intensities are $8 \times 10^{14}$ W/cm$^2$ (solid) and $1 \times 10^{15}$ W/cm$^2$ (dotted); for the $\alpha = 2$ drives, peak intensity is $1 \times 10^{15}$ W/cm$^2$ (dashed curve).

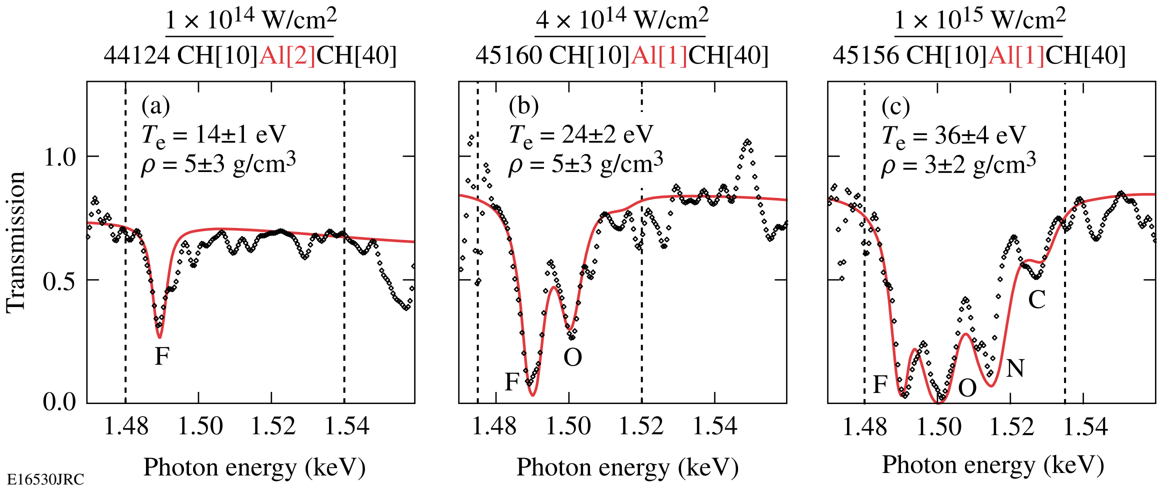

Figure 116.28
Measured Al absorption spectra (diamonds) and fits (solid curve) during shock heating and compression for the square laser pulse drives having intensities of (a) $1 \times 10^{14}$ W/cm$^2$, (b) $4 \times 10^{14}$ W/cm$^2$, and (c) $1 \times 10^{15}$ W/cm$^2$. The buried depth of an Al layer was 10 $\mu$m for all three targets. The inferred condition from the fit is shown in each figure.

the highest drive intensity ($1 \times 10^{15}$ W/cm$^2$). Consequently, the inferred electron temperature increased from 14 eV to 24 eV to 36 eV (with 10% errors) as the drive intensities increased from $1 \times 10^{14}$ W/cm$^2$ to $4 \times 10^{14}$ W/cm$^2$ to $1 \times 10^{15}$ W/cm$^2$. The mass densities inferred from measured spectra for the square laser pulses were ~5 g/cm$^3$ (±~2 g/cm$^3$).

Three buried depths—5, 10, and 15 $\mu$m—of the Al layer were studied for the 1-ns square pulse drive with a peak intensity of $1 \times 10^{15}$ W/cm$^2$. A time history of the electron temperature in the Al layer inferred from the absorption spectroscopy for each of these buried depths is plotted in Fig. 116.29. The experimental data are presented with a single symbol during shock-wave heating and with a vertical line connecting two symbols that represent the range of upper and lower limits of inferred $T_e$ after the heat front penetrates. Figure 116.29 also shows the *LILAC* simulations using $f = 0.06$, $f = 0.1$, and the nonlocal model. The post-processed electron temperatures were calculated as described in the previous section. The shock-breakout time from the rear surface of the target ($t = 0.72$ ns),

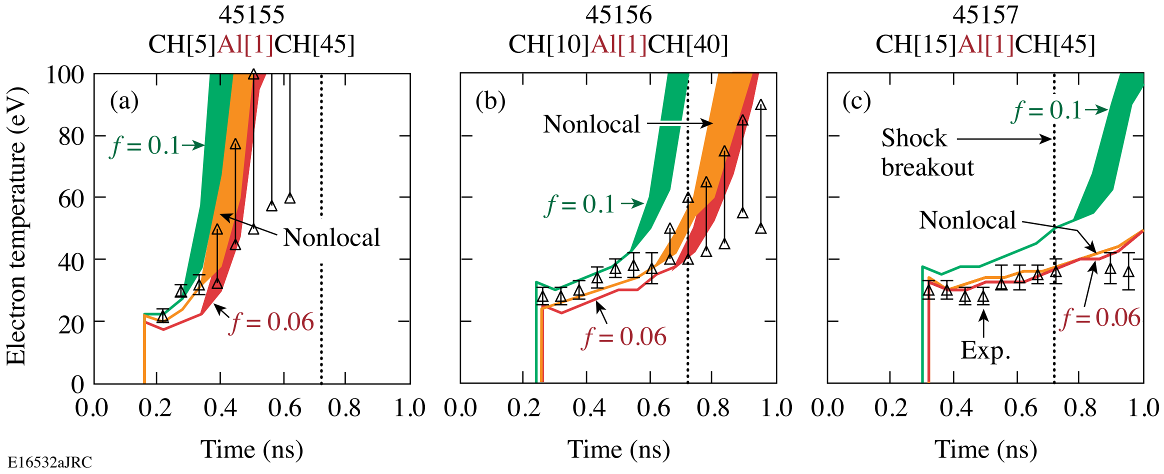

Figure 116.29
Time-resolved electron temperatures in the buried Al layer inferred from the experiment (triangles) for a 1-ns square laser drive with an intensity of $1 \times 10^{15}$ W/cm$^2$ compared with the *LILAC* simulations using $f = 0.06$ (dark gray), $f = 0.1$ (black), and the nonlocal model (light gray). The depth of the buried Al layer was (a) 5 $\mu$m, (b) 10 $\mu$m, and (c) 15 $\mu$m. The shock-breakout time from the rear surface of the target ($t = 0.72$ ns), calculated with the nonlocal model for this drive intensity, is indicated by the dotted vertical line in each figure.

calculated with the nonlocal model for this drive intensity, is indicated by the dotted vertical line in each figure. The drive foil begins to accelerate and decompress after the shock wave breaks out of the rear surface of the target. An examination of Fig. 116.29 reveals the experimental delay in the onset of shock-wave heating as the buried depth of the Al layer is increased. A similar trend is observed for heat-front penetration. The simulation with the higher flux limiter predicts more shock-wave heating and an earlier penetration of the heat front than the other models. While the shock wave is transiting the drive foil (i.e., for times earlier than the shock-breakout time at $t = 0.72$ ns), the *LILAC* predictions using the nonlocal model agree with the experimental results for the 5-$\mu$m, 10-$\mu$m, and 15-$\mu$m buried depths. The nonlocal prediction is closer to the $f = 0.1$ prediction for the 5-$\mu$m buried depth, but it is similar to the $f = 0.06$ prediction for the deeper depths. This shows the time-dependent nature of the nonlocal heat transport.[46] For the 5-$\mu$m and 10-$\mu$m buried depths, the measured timing of heat-front penetration occurs before or around the predicted shock-breakout time. The prediction using the nonlocal model or $f = 0.06$ agrees with the measured heat-front penetration of the 5-$\mu$m and 10-$\mu$m buried depths. After the shock-wave breakout there are some minor discrepancies between the models and the measurements. The measured electron temperature for the 15-$\mu$m buried depth remains constant in time, while the prediction shows it should increase with time although it is close to the uncertainties. This discrepancy is likely due to the 2-D effects discussed in the next section. The $f = 0.1$ predictions do not agree with the measured heat-front penetration in the 10-$\mu$m- and 15-$\mu$m-buried-depth cases.

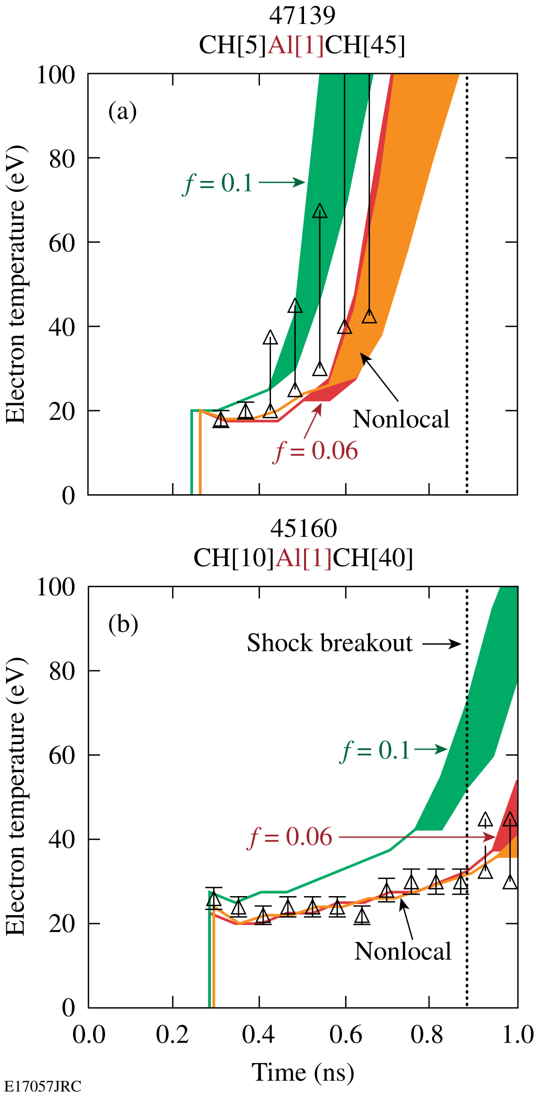

Figure 116.30
Time-resolved electron temperatures in the buried Al layer inferred from the experiment (triangles) for a 1-ns square laser drive with an intensity of $4 \times 10^{14}$ W/cm$^2$ for (a) 5-$\mu$m and (b) 10-$\mu$m buried depths. The data are compared with *LILAC* simulations using $f = 0.06$ (dark gray), $f = 0.1$ (black) and the nonlocal model (light gray). The shock-breakout time from the rear target surface ($t = 0.88$ ns) is calculated with the nonlocal model for this drive intensity and is indicated by the dotted vertical line in each figure.

Two buried depths—5 and 10 $\mu$m—of the Al layer were studied for the 1-ns square pulse drive with a peak intensity of $4 \times 10^{14}$ W/cm$^2$. A time history of the electron temperature in the Al layer inferred from the absorption spectroscopy for each of these buried depths is plotted in Fig. 116.30. The experimental data are presented with a single symbol during shock-wave heating and with a vertical line connecting two symbols that represent the range of upper and lower limits of inferred $T_e$ after the heat front penetrates. Figure 116.30 also shows the *LILAC* simulations using $f = 0.06$, $f = 0.1$, and the nonlocal model. The post-processed electron temperatures were calculated as described in the previous section. The shock-breakout time from the target's rear surface ($t = 0.88$ ns) is calculated with the nonlocal model for this drive intensity and is indicated by the dotted vertical line in each figure. It occurs very late in the pulse. Timing of shock-wave heating and heat-front penetration on the buried depth is similar to Fig. 116.29. Nonlocal predictions are similar to those using $f = 0.06$. The simulation with the higher flux limiter predicts more shock-wave heating and an earlier penetration of the heat front than the other models. *LILAC* predictions using the nonlocal model or the $f = 0.06$ model agree with the experimental results for the 10-$\mu$m buried depth throughout the pulse. The initial level of shock-wave heating agrees with all three models for the 5-$\mu$m buried depth; however, the $f = 0.1$ model is closest to the heat-front penetration for this shallow depth. The advanced penetration of the heat front for the 5-$\mu$m buried depth may be caused by spatial nonuniformities in the laser irradiation profile.

Two buried depths—5 and 10 $\mu$m—of the Al layer were studied for the 3-ns square pulse drive with a peak intensity of $1 \times 10^{14}$ W/cm$^2$. The 2-D SSD system was not employed for this experiment to match the drive conditions used for the spectrally resolved x-ray scattering measurement presented in Ref. 22. Smoothing by spectral dispersion smoothes the spatial nonuniformities in the laser irradiation profile on a time scale that is short compared to the hydrodynamic time scales. The disadvantage of turning off 2-D SSD is an increase in the level of the laser irradiation nonuniformities. A time history of the electron temperature in the Al layer inferred from the absorption spectroscopy for each of these buried depths is shown in Fig. 116.31. The experimental data are presented with a single symbol during shock-wave heating and with a vertical line connecting two symbols that represent the range of upper and lower limits of inferred $T_e$ after the heat front penetrates. Figure 116.31 also shows the *LILAC* simulations using $f = 0.06$, $f = 0.1$, and the nonlocal model. The post-processed electron temperatures were calculated as described in the previous section. The shock-breakout time ($t = 1.37$ ns) calculated with the nonlocal model for this drive intensity is indicated by the dotted vertical line in each figure. All of the models have similar predictions. The *LILAC* predictions agree with the experimental results for the 10-$\mu$m buried depth throughout the pulse [Fig. 116.31(b)]. This drive appears to be insensitive to the reduction of radiative heating caused by 2-D effects. The coronal plasma temperature predicted with *LILAC* remains relatively low (~2 keV) after shock-breakout time; consequently, the level of radiative heating is negligible. The initial level of shock-wave heating for the 5-$\mu$m buried depth is below detection threshold until just after $t = 0.4$ ns. The heat-front penetration for this shallow depth is much earlier than the *LILAC* predictions [Fig. 116.31(a)] and is most likely caused by the higher level of laser irradiation nonuniformities with the 2-D SSD turned off. The 10-$\mu$m buried depth does not appear to be influenced by this effect. Plasma smoothing of the laser irradiation nonuniformities reduces nonuniformities in the drive at the ablation surface.[47] Since the heat-front penetration time is delayed as the buried depth is increased, the 10-$\mu$m buried depth has more time to form a coronal plasma. Consequently, the plasma smoothing is more effective and early heat-front penetration is not observed for the 10-$\mu$m case. Further investigation to understand the cause of the early heat-front penetration for this drive condition is needed. The measured level of shock-wave heating of ~13 eV for the 3-ns square pulse drive with a peak intensity of $1 \times 10^{14}$ W/cm$^2$ is close to the simulations. This is consistent with the results from noncollective spectrally resolved x-ray scattering experiment on OMEGA using the same drive condition.[22]

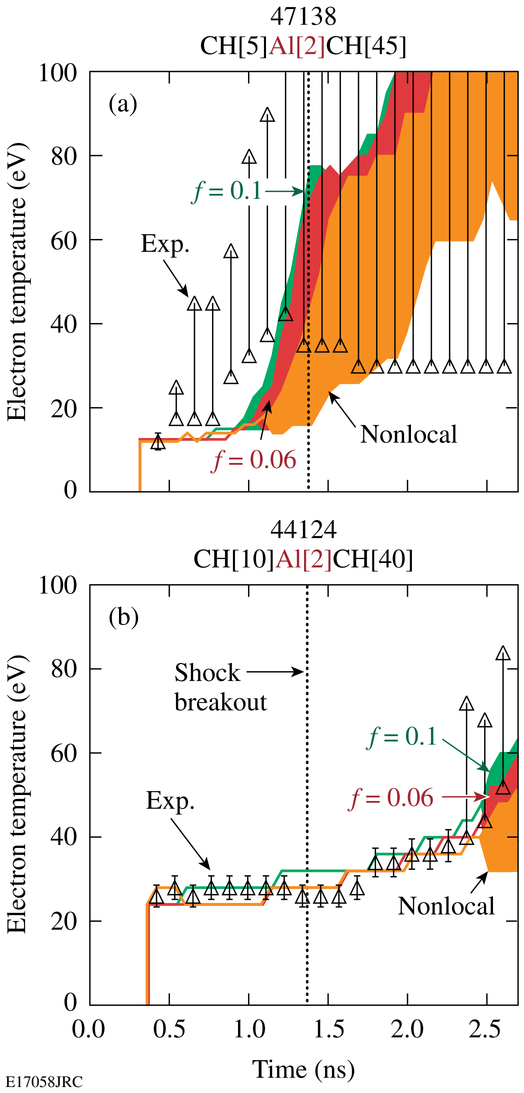

Figure 116.31
Comparisons of time-resolved electron temperatures in the buried Al layer inferred from the experiment (triangles) for a 3-ns square laser drive with an intensity of $1 \times 10^{14}$ W/cm$^2$ with the *LILAC* simulations using $f = 0.06$ (dark gray), $f = 0.1$ (black), and the nonlocal model (light gray) for (a) 5-$\mu$m and (b) 10-$\mu$m buried depths. The shock-breakout time ($t = 1.37$ ns) calculated with the nonlocal model for this drive intensity is indicated by the dotted vertical line in each figure.

2. Plasma Conditions Achieved with Shaped Laser Pulses

High target compression can be achieved in ICF using a shaped laser pulse drive that launches a weak shock wave during the foot pulse through the target followed by a compression wave during the rise to the main pulse. Three shaped laser drives were investigated using the following laser pulse shapes: $\alpha = 3$ drive with a peak intensity of $8 \times 10^{14}$ W/cm$^2$, $\alpha = 3$ drive with a peak intensity of $1 \times 10^{15}$ W/cm$^2$, and $\alpha = 2$ drive with a peak intensity of $1 \times 10^{15}$ W/cm$^2$ [see Fig. 116.27(b)]. To realize the full effect of the compression wave on the buried Al layer in a planar target, the shock-breakout time needs to occur after the shaped laser pulse reaches peak intensity. The buried depth should be deep enough to avoid heat-front penetration until after the compression wave has propagated through the Al layer. This section demonstrates how higher target compression can be achieved with a shaped laser drive compared to a square laser drive.

The peak intensity of the $\alpha = 3$ drive was increased from $8 \times 10^{14}$ W/cm$^2$ to $1 \times 10^{15}$ W/cm$^2$ to investigate preheat of the buried Al layer by energetic electrons. The higher peak intensities were achieved by increasing the number of drive beams from 15 to 21. In the TPD instability,[11] the incident laser decays into two electron-plasma waves (plasmons) around the quarter-critical-density region, producing energetic electrons.[48] Preheat caused by these electrons usually occurs during the main drive of the shaped laser pulse.[49] Hard x-ray signals produced by the energetic electrons have been observed to increase exponentially with the overlapped laser intensities in the range from 0.5 to $1.0 \times 10^{15}$ W/cm$^2$ range (Ref. 49). This experiment was designed to increase the energetic electron production by varying the peak intensity of the $\alpha = 3$ drive. The hard x-ray signals were monitored with the four-channel hard x-ray detector recording x-ray energies greater than 20 keV, 40 keV, 60 keV, and 80 keV (Ref. 49). In the absorption spectroscopy experiment, hard x rays can be produced in the coronal plasmas of the backlighter and the drive foil. Hard x-ray measurements of the drive foil alone are not available.

TPD is expected to occur for most of the drives under consideration based on the threshold parameter[48] given as $I_{14} \times L_{\mu\text{m}} \big/ (230 \times T_{\text{c}})$, where $I_{14}$ is the incident laser intensity at the quarter-critical density in units of $10^{14}$ W/cm$^2$, $L_{\mu\text{m}}$ is the density scale length in microns at the quarter-critical density, and $T_{\text{c}}$ is the electron temperature at the quarter critical density in keV. When the threshold parameter is above 1, laser light from the drive may decay into two electron-plasma waves around the quarter-critical density. The predicted density scale length in a planar target is longer than in a spherical implosion with the same overlapped laser intensity, resulting in more-energetic electron production. The higher-intensity $\alpha = 3$ drive exceeds a threshold parameter of 1 at $t = {\sim}0.8$ ns, while the threshold parameter for the lower-intensity drive exceeds 1 around $t = 1.0$ ns.

Three buried depths—10, 15, and 20 $\mu$m—of the Al layer were studied for the $\alpha = 3$ drive with peak intensity of $8 \times 10^{14}$ W/cm$^2$. A time history of the electron temperature in the Al layer inferred from the absorption spectroscopy for each of these buried depths is plotted in Fig. 116.32. The experimental data are presented with a single symbol during shock-wave

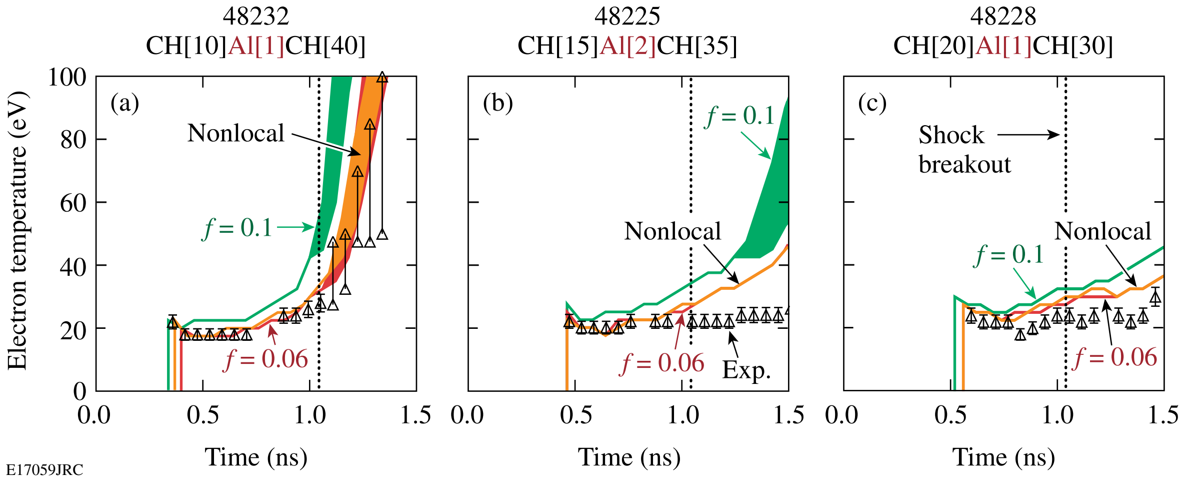

Figure 116.32
Comparisons of the measured electron temperatures in the buried Al layer (triangles) for the $\alpha = 3$ drive with peak intensity of $8 \times 10^{14}$ W/cm$^2$ with the *LILAC* simulations using $f = 0.06$ (dark gray), $f = 0.1$ (black), and the nonlocal model (light gray) for (a) 10-$\mu$m, (b) 15-$\mu$m, and (c) 20-$\mu$m buried depths. The shock-breakout time ($t = 1.04$ ns) calculated with the nonlocal model for this drive intensity is indicated by the dotted vertical line in each figure.

heating and with a vertical line connecting two symbols that represent the range of upper and lower limits of inferred $T_e$ after the heat front penetrates. Figure 116.32 shows the *LILAC* simulations using $f = 0.06$, $f = 0.1$, and the nonlocal model. The post-processed electron temperatures were calculated as described in the previous section. The timing of shock-wave heating and heat-front penetration is delayed as the buried depth of the Al layer is increased. The shock-breakout time ($t$ = 1.04 ns) calculated with the nonlocal model for this drive intensity is indicated by the dotted vertical line in each figure. As can be seen in Fig. 116.27(b) the rising edge of the main drive of the $\alpha = 3$ drive with a peak intensity of $8 \times 10^{14}$ W/cm$^2$ ends at 1.2 ns, which is after the shock-breakout time ($t$ = 1.04 ns). While the shock wave is transiting the drive foil (i.e., for times earlier than the shock-breakout time at $t$ = 1.04 ns), *LILAC* predictions using the nonlocal model or the $f = 0.06$ model agree with the experimental results for the 10-$\mu$m, 15-$\mu$m, and 20-$\mu$m buried depths. The $f = 0.1$ prediction is higher than the electron temperature inferred from the experiment during shock heating, and the predicted heat-front penetration occurs earlier than the experimental results. In Fig. 116.32(a) the *LILAC* predictions using the nonlocal model or the $f = 0.06$ model agree with the measured timing of heat-front penetration that occurs just after the shock-breakout time. The late time discrepancies observed in Figs. 116.32(b) and 116.32(c) are likely due to 2-D effects discussed below.

Similar plasma conditions were inferred in CH/Al/CH targets driven with the $\alpha = 3$ drive with a higher peak intensity of $1 \times 10^{15}$ W/cm$^2$. The time-resolved electron temperatures in the Al layer inferred are presented in Fig. 116.33 for buried depths of 15 $\mu$m and 20 $\mu$m. The 10-$\mu$m depth was not studied with the higher drive intensity because the Al layer is ablated before peak compression is achieved in the target. The experimental data and the *LILAC* simulations in Fig. 116.33 are presented in a format similar to Fig. 116.32. The shock-breakout time ($t$ = 1.02 ns) calculated by the nonlocal model for this drive intensity is indicated by the dotted vertical line in each figure. While the shock wave is transiting the drive foil (i.e., for times earlier than the shock-breakout time at $t$ = 1.02 ns), *LILAC* predictions using the nonlocal model or the $f = 0.06$ model are close to the experimental results for the 15-$\mu$m and 20-$\mu$m buried depths. Prior to the shock-breakout time, however, the higher-intensity drive with the 20-$\mu$m buried depth shows slightly more discrepancy between simulation and measurement [see Fig. 116.33(b)] than the same case with the lower-intensity drive [see Fig. 116.32(c)]. The electron temperature predicted with $f = 0.1$ is higher than that measured for all times.

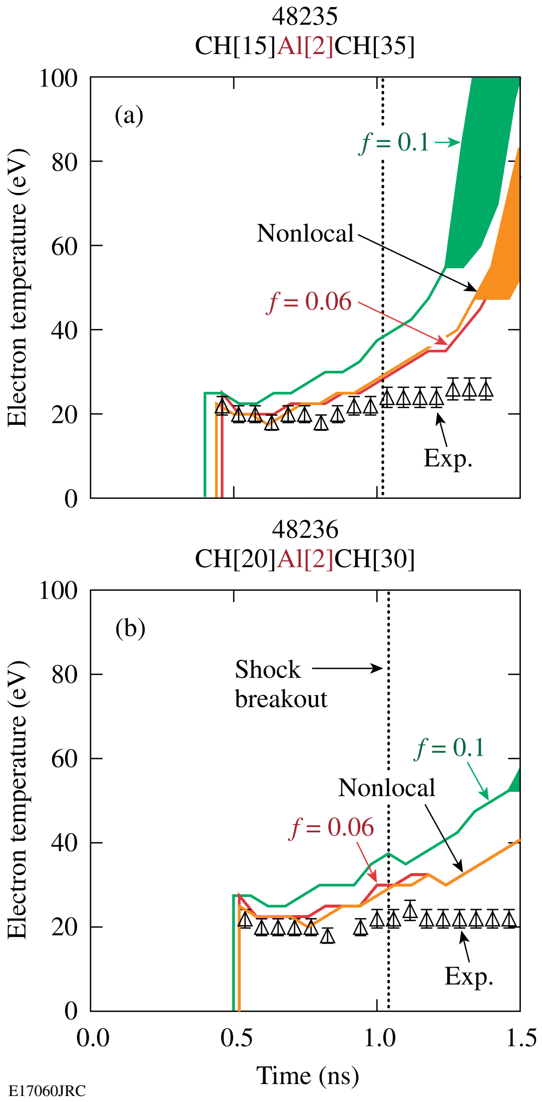

Figure 116.33
Comparisons of the measured electron temperatures in the buried Al layer (triangles) for the $\alpha = 3$ drive with a peak intensity of $1 \times 10^{15}$ W/cm$^2$ with the *LILAC* simulations using $f = 0.06$ (dark gray), $f = 0.1$ (black), and the nonlocal model (light gray) for (a) 15-$\mu$m and (b) 20-$\mu$m buried depths. The shock-breakout time ($t$ = 1.02 ns) calculated with the nonlocal model for this drive intensity is indicated by the dotted vertical line in each figure.

After the shock wave breaks out of the rear surface of the target, the *LILAC* simulation does not accurately predict the experimental results. This can be seen in Figs. 116.32(b), 116.32(c), 116.33(a), and 116.33(b). Although rising electron temperatures are predicted for 15- and 20-$\mu$m depths due to radiative heating, the experimental data remain at a constant value of ~20 eV. Measured and simulated absorption spectra are examined for times before and after the shock-wave breakout time in Fig. 116.34.

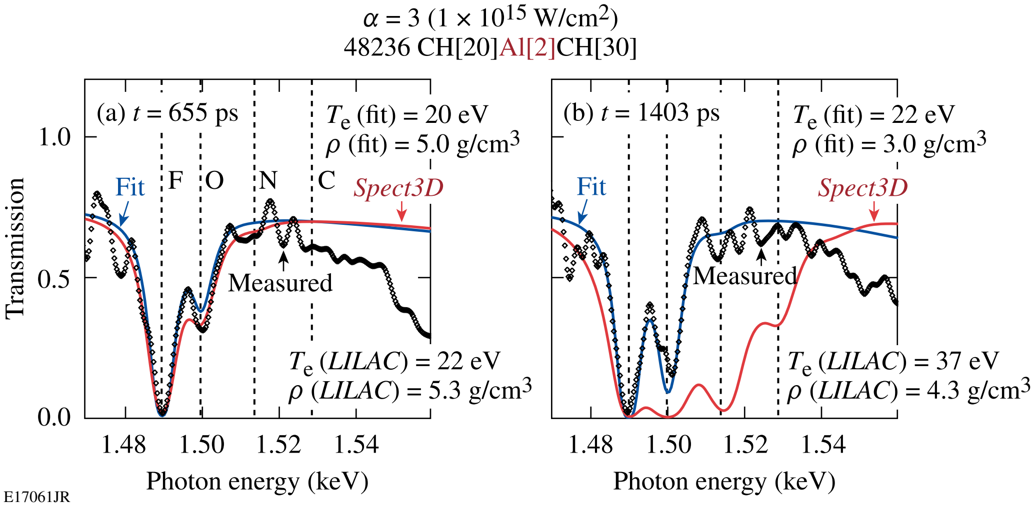

Figure 116.34
Measured (diamonds) and simulated Al absorption spectra before and after the shock-breakout time for the $\alpha = 3$ drives with a peak intensity of $1 \times 10^{15}$ W/cm$^2$ (shot 48236). The fitted spectra assuming uniform conditions are shown in gray and *LILAC*/*Spect3D* spectra in black.

The simulated spectra are calculated using *LILAC* and *Spect3D* as described in **One-Dimensional Simulations** (p. 187). The spectral fitting calculated with *PrismSpect* is also shown. The simulated absorption spectrum is close to the measured one before shock breakout, for the $\alpha = 3$ drive with peak intensity of $1 \times 10^{15}$ W/cm$^2$ [Fig. 116.34(a)], but after shock breakout, the measured spectrum has virtually no N-like and C-like absorption features indicating a lower electron temperature than the simulated one [Fig. 116.34(b)]. Quantitatively, the $T_e$ and $\rho$ inferred from the spectral fitting are 20 eV and 5.0 g/cm$^3$ and compare favorably to the predicted conditions of 22 eV and 5.3 g/cm$^3$. After the shock breakout, the $T_e$ and $\rho$ inferred from the spectral fitting are 22 eV and 3.0 g/cm$^3$ and are lower than the predicted conditions of 37 eV and 4.3 g/cm$^3$. If the mass density in the fits were increased, the peak of the O-like absorption is predicted to increase in transmission. Therefore, the differences between the simulated and measured spectra can be explained only by a lower measured electron temperature compared to the prediction.

The significant discrepancies between the measured and predicted plasma conditions in the Al layer after the shock wave breaks out of the rear surface of the foil are attributed to 2-D effects in the planar experimental geometry. The laser drive does not produce a planar shock front. The spatial-intensity profile of the laser drive incident on the target is defined by the single-beam super-Gaussian profile[50] and the overlap of beams having an angle of incidence up to ~60°. It causes the ablation front to have curvature and it creates a coronal plasma with lateral gradients in the temperature and density profiles, leading to a lateral heat flow. The resulting lower coronal plasma temperatures reduce the radiated x-ray power of the corona compared to the case with only radial gradients (i.e., the 1-D prediction). As a consequence the radiative heating of the Al layer is reduced. Nonuniform acceleration of the drive foil can bow the target, further enhancing the 2-D effects.

A 2-D hydrodynamic simulation *DRACO*[51] was performed to estimate the amount of lateral heat flow caused by 2-D effects. Figure 116.35 shows the simulated mass-density contours from *DRACO* for the $\alpha = 3$ with a peak intensity of $1 \times 10^{15}$ W/cm$^2$ at (a) $t = 0$ ns, (b) $t = 0.6$ ns, and (c) $t = 1.4$ ns. The calculation was performed with cylindrical symmetry around the horizontal axis and the laser is incident on the target from the right. The vertical axis corresponds to the radial dimension of the target. The Al 1*s*–2*p* absorption spectroscopy probes radial locations up to 200 $\mu$m, which corresponds to the uniform drive region. The 2-D simulation includes the experimental configuration of beam angles and the single-beam intensity profiles. At $t = 0.6$ ns, curvature in the shock front and deformation of the shocked planar target are evident. The curvature becomes more pronounced at $t = 1.4$ ns. This creates 2-D gradients in the temperature and density profile in the coronal plasma, leading to a lateral heat flow. Figure 116.36 compares 1-D *LILAC* and 2-D *DRACO* simulations for (a) the maximum corona plasma temperatures and (b) the electron temperatures in the Al layer along with the measurement. The 2-D simulation shows a lower corona plasma temperature by ~1 keV and a lower electron temperature in the buried Al layer by ~10 eV than the 1-D simulation at the 1-D predicted time of shock breakout ($t$ = 1.02 ns). The minimum and maximum temperatures in the Al layer predicted by the 2-D simulation are closer to the experimental results than the 1-D prediction as shown in Fig. 116.36(b).

Preheat by energetic electrons is expected to be observed in the drive foil having the Al layer buried at 20 $\mu$m and driven with the $\alpha$ = 3 drive with a peak intensity of $1 \times 10^{15}$ W/cm$^2$ [Fig. 116.34(b)]. The 1-D *LILAC* prediction does not simulate the TPD instability; therefore, evidence of preheat would be an

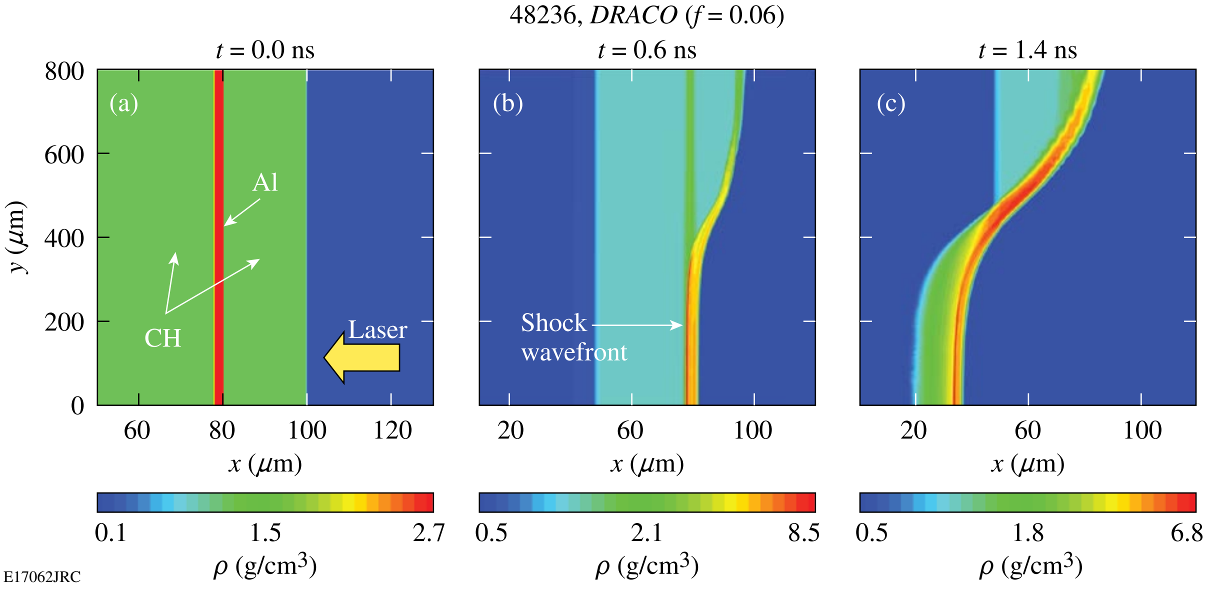

Figure 116.35
Mass-density contours of the driven CH/Al/CH planar target simulated with 2-D hydrodynamics code *DRACO* for shot 48236 at (a) $t$ = 0, (b) $t$ = 0.6 ns, and (c) $t$ = 1.4 ns. The calculation was performed with cylindrical symmetry around the horizontal axis and the laser is incident on the target from the right.

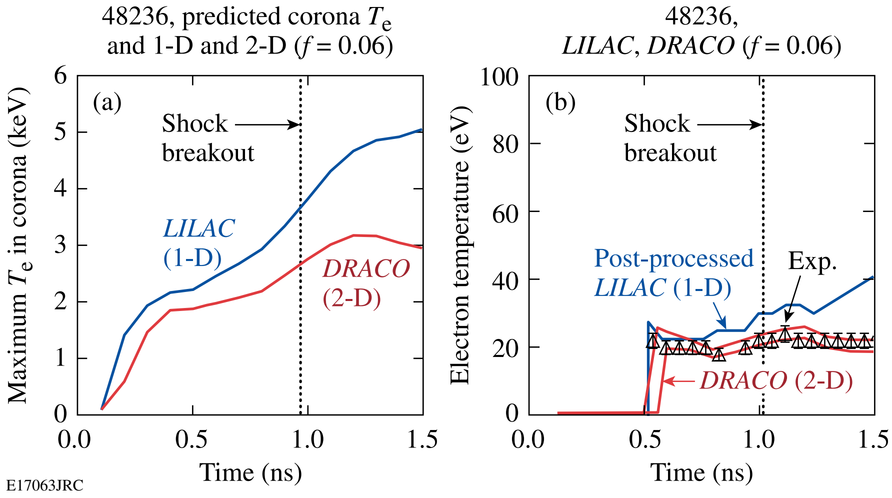

Figure 116.36
(a) A comparison of the maximum coronal plasma temperatures predicted by 1-D and 2-D simulations for a planar CH/Al/CH target driven with the $\alpha$ = 3 drive with a peak intensity of $1 \times 10^{15}$ W/cm$^2$. (b) Time histories of predicted electron temperatures in the Al layer using *LILAC* and *DRACO* compared with the experimental data for shot 48236. The 1-D, post-processed $T_e$ is shown in black, and the minimum and maximum predicted temperatures with *DRACO* are shown in gray.

inferred electron temperature in the Al layer that is higher than 1-D prediction. The 2-D effects, however, cause the electron temperature in the Al layer to be less than the 1-D prediction after the shock-breakout time ($t = 1.04$ ns). The 2-D effects mask any signature of increased electron temperature due to preheat from energetic electrons late in the drive pulse. Therefore, the evidence for preheat due to energetic electrons is inconclusive in this experiment.

Three buried depths—10, 15, and 20 $\mu$m—of the Al layer were studied for the $\alpha = 2$ drive with a peak intensity of $1 \times 10^{15}$ W/cm$^2$. A time history of the electron temperature in the Al layer inferred from the absorption spectroscopy for each of these buried depths is plotted in Fig. 116.37. The experimental data are presented with a single symbol during shock-wave heating and with a vertical line connecting two symbols that represent the range of upper and lower limits of inferred $T_e$ after the heat front penetrates. The foot intensity of the $\alpha = 2$ drive pulse was ~$4 \times 10^{13}$ W/cm$^2$ [Fig. 116.27(b)], producing ~8-Mbar pressure in the Al layer. The shock-wave strength was too weak to increase the $T_e$ in the Al layer enough to generate F-like Al; however, a shifting spectral position of the Al K edge was observed. The absolute timing of the measurement could be established with the shifting Al K edge. The observed Al 1*s*–2*p* absorption lines appeared as the electron temperature in the Al layer increased due to radiative heating during the main laser drive and the compression wave. Figure 116.37 shows *LILAC* simulations using $f = 0.06$, $f = 0.1$, and the nonlocal model. The post-processed electron temperatures were calculated as described in the previous section. The timing of shock-wave heating and heat-front penetration are delayed as the buried depth of the Al layer is increased. The shock-breakout time ($t = 1.6$ ns) calculated with the nonlocal model for this drive intensity is indicated by the dotted vertical line in each figure. As can be seen in Fig. 116.27 the rising edge of the main drive of the $\alpha = 2$ drive with a peak intensity of $1 \times 10^{15}$ W/cm$^2$ ends at 1.5 ns, which is just before the shock-breakout time ($t = 1.6$ ns). The predicted peak compression of the Al occurs at 1.5 ns. *LILAC* simulations with different thermal-transport models are close to each other for this drive condition. The *LILAC* simulations accurately model the experimental data before shock-breakout time of 1.6 ns. The inferred mass density from the Stark-broadened spectrum at the peak compression is 11 g/cm$^3$ (±5 g/cm$^3$). As described before, the 2-D effects lower the electron temperature in the coronal plasma, reducing the radiative heating of the Al. The 2-D predictions for 15- and 20-$\mu$m depths are in good agreement with the measurements before the shock-breakout times, but lower than the measurements by ~5 eV after the shock breakout. The TPD threshold parameter for the $\alpha = 2$ drive exceeds 1 at $t = 1.3$ ns, indicating that the difference between the measured and 2-D predicted temperatures in the Al at late time of the drive could be heating due to energetic electrons from the TPD instability. Further work is required to identify the level of preheating and to include the nonlocal electron thermal transport model in the 2-D simulations for a consistent explanation of the experimental results for the square and shaped laser drives after the shock-breakout time.

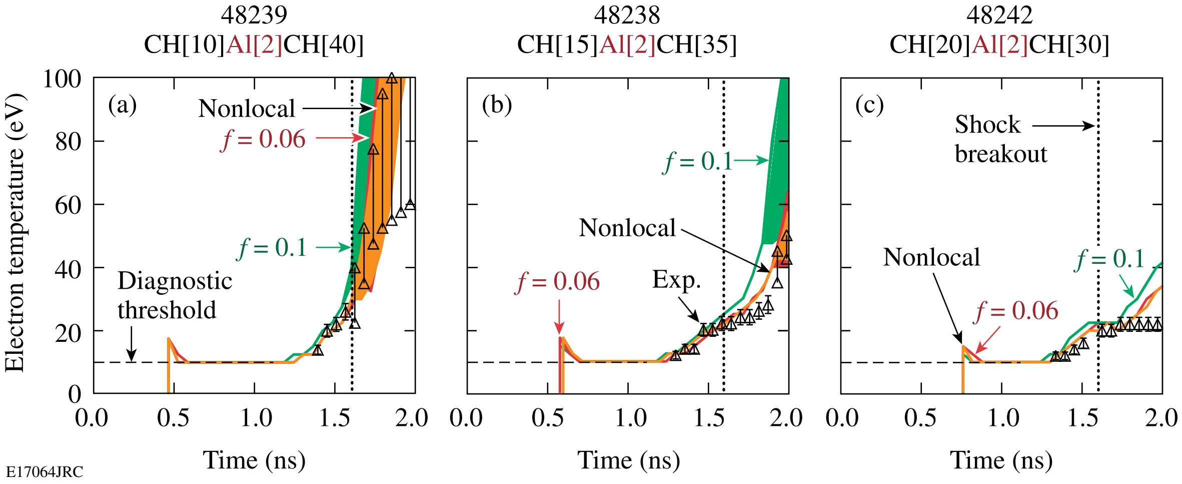

Figure 116.37
Comparisons of the measured electron temperatures in the buried Al layer for the $\alpha = 2$ drive with *LILAC* simulations using $f = 0.06$ (dark gray), $f = 0.1$ (black), and the nonlocal model (light gray) for (a) 10-$\mu$m, (b) 15-$\mu$m, and (c) 20-$\mu$m buried depths. The shock-breakout time ($t = 1.6$ ns) calculated with the nonlocal model for this drive intensity is indicated by the dotted vertical line in each figure.

Higher target compression has been achieved with a shaped laser pulse drive compared to a square laser pulse drive. A single shock wave launched by the square laser pulse creates a nearly constant mass density in the shocked Al. The shaped laser pulse launches a shock wave by the foot laser intensity and multiple hydrodynamic waves coalescing to form a compression wave with increasing pressure during the ramp of the laser intensity. A mass density of 11 g/cm$^3$ (±5 g/cm$^3$) and an electron temperature of 20 eV were created in the buried Al layer with the $\alpha = 2$ drive. Figure 116.38 presents a comparison of Al 1$s$–2$p$ absorption spectra for two drive conditions. Both spectra have F-like and O-like absorption features. This is the first measurement of the plasma temperature and density in a direct-drive target created by multiple shock waves (i.e., a weak shock and a compression wave).[24] The best fit to each spectrum is represented by the black curve. The mass densities inferred are between 5 and 7 g/cm$^3$ for the 1-ns square laser pulse [Fig. 116.38(a)] and between 6 and 16 g/cm$^3$ for the $\alpha =$ 2 drives [Fig. 116.38(b)]. The simulated spectra for the upper and lower limits of the mass density are plotted in Fig. 116.38. The predicted mass density of 14 g/cm$^3$ is consistent with the measured density of 11 g/cm$^3$ at the peak compression for the shaped laser pulse. The lower predicted mass density of 8 g/cm$^3$ for the 1-ns square pulse is consistent with the lower inferred value of 6 g/cm$^3$. Although the difference in the mass densities is just resolved with the Al 1$s$–2$p$ absorption spectroscopy, this experiment shows that higher target compression is achieved with the shaped laser pulse drive compared with the square laser pulse drive.

## Future Work and Application

The experimental results presented here demonstrate the diagnostic capability of measuring shock-wave heating and timing of heat-front penetration using the time-resolved Al 1$s$–2$p$ absorption spectroscopy of a direct-drive, shock-wave–heated and compressed planar plastic foil for a wide range of drive conditions. Understanding electron thermal transport in a spherical geometry is the ultimate goal of this research. A spherical or hemispherical CH target with a buried Al layer will be investigated. Shifting to a spherical geometry eliminates the 2-D effects observed in the planar geometry and would pave the way for a conclusive preheat experiment. The CH foil is a surrogate for a deuterium–tritium (DT) cryogenic layer for a direct-drive ICF capsule. Measurements of plasma conditions in a shock-wave–heated planar DT or DD cryogenic layer with x-ray absorption spectroscopy will be a next step to understanding the shell condition of a laser-driven cryogenic ICF target. The target development will be challenging since a direct-drive, cryogenic deuterium planar experiment using x-ray absorption spectroscopy will require an Al foil in a liquid deuterium.

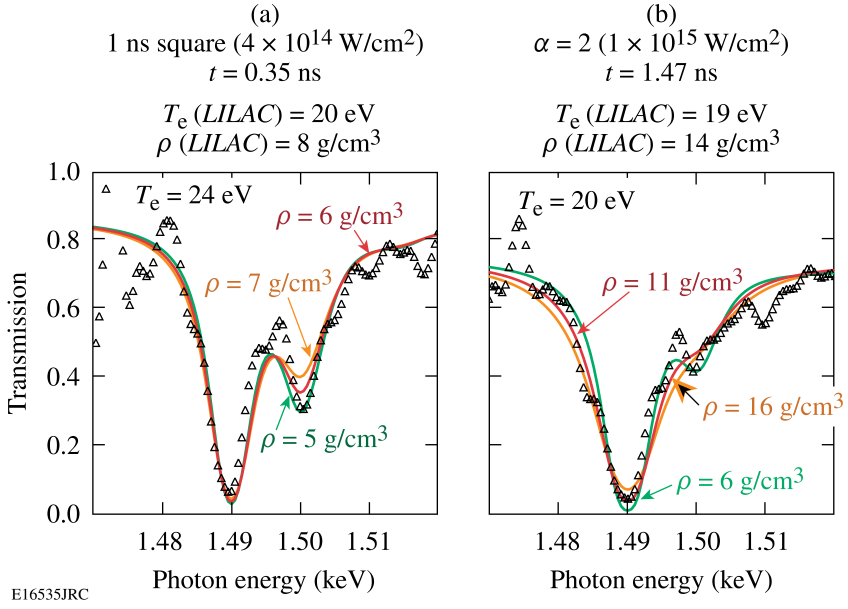

Figure 116.38
Spectral fits to the measured spectra for (a) a square laser pulse (4 × 10$^{14}$ W/cm$^2$) taken at $t$ = 0.35 ns and (b) shaped laser pulse ($\alpha$ = 2 drive) taken at 1.47 ns. Inferred mass densities from fitting the Stark-broadened Al 1$s$–2$p$ absorptions are between 5 g/cm$^3$ (light gray) and 7 g/cm$^3$ (dark gray) for the square laser pulse and between 6 g/cm$^3$ (light gray) and 16 g/cm$^3$ (dark gray) for the shaped laser pulse. The modeled spectra for the best fit are shown in black.

## Conclusion

The plasma conditions of a direct-drive, shock-wave–heated and compressed planar target comprising warm dense matter[13] were diagnosed using time-resolved Al 1*s*–2*p* absorption spectroscopy. A 50-$\mu$m planar CH foil with a buried tracer layer of Al was irradiated with intensities of $10^{14}$ to $10^{15}$ W/cm$^2$, and ~1.5 keV x rays from a point-source Sm backlighter were transmitted through the drive foil. Local shell conditions of $T_e$ and $\rho$ during the shock-wave heating and heat-front penetration were inferred from the measured absorption spectra analyzed with *PrismSPECT*, assuming uniform conditions in the Al layer. The drive foil was simulated with the 1-D hydrodynamic code *LILAC* using flux-limited ($f = 0.1$ and $f = 0.06$) or a nonlocal thermal transport model. The experimental results showed that 1-D simulations using the nonlocal model or $f = 0.06$ accurately predict the timing of heat-front penetration and the level of shock-wave heating for square and shaped laser pulses while the shock transits the target. The accuracy of the electron temperatures inferred from the experiments was sufficient to distinguish between the two flux-limited hydrodynamics predictions. The predicted plasma conditions of a shocked Al layer using the nonlocal model were similar to the ones using $f = 0.06$ in this experiment. Significant discrepancies between measured and predicted shock-wave heating were observed at late times in the drive, which can be explained by reduced radiative heating due to lateral heat flow in the corona. An early burnthrough observed for 5-$\mu$m buried depth could be caused by high laser irradiation nonuniformity levels without laser-beam smoothing with 2-D SSD. Preheat experiments of the buried Al layer due to energetic electron production by the two-plasmon-decay instability were inconclusive since the 2-D effects masked any experimental signature of preheat.

## ACKNOWLEDGMENT

The authors are grateful to M. J. Bonino and S. G. Noyes for their target fabrication expertise and to R. E. Bahr and S. Mott for diagnostic expertise as well as to the OMEGA operations crew for providing the highly reproducible laser performance. The authors appreciate the insightful discussions with A. Ng and D. Hoarty. This work was supported by the U.S. Department of Energy Office of Inertial Confinement Fusion under Cooperative Agreement No. DE-FC52-08NA28302, the University of Rochester, and the New York State Energy Research and Development Authority. The support of DOE does not constitute an endorsement by DOE of the views expressed in this article.

## REFERENCES

1. J. Nuckolls *et al.*, Nature **239**, 139 (1972); J. D. Lindl, R. L. McCrory, and E. M. Campbell, Phys. Today **45**, 32 (1992); R. L. McCrory, J. M. Soures, C. P. Verdon, F. J. Marshall, S. A. Letzring, S. Skupsky, T. J. Kessler, R. L. Kremens, J. P. Knauer, H. Kim, J. Delettrez, R. L. Keck, and D. K. Bradley, Nature **335**, 225 (1988); R. L. McCrory, S. P. Regan, S. J. Loucks, D. D. Meyerhofer, S. Skupsky, R. Betti, T. R. Boehly, R. S. Craxton, T. J. B. Collins, J. A. Delettrez, D. Edgell, R. Epstein, K. A. Fletcher, C. Freeman, J. A. Frenje, V. Yu. Glebov, V. N. Goncharov, D. R. Harding, I. V. Igumenshchev, R. L. Keck, J. D. Kilkenny, J. P. Knauer, C. K. Li, J. Marciante, J. A. Marozas, F. J. Marshall, A. V. Maximov, P. W. McKenty, J. Myatt, S. Padalino, R. D. Petrasso, P. B. Radha, T. C. Sangster, F. H. Séguin, W. Seka, V. A. Smalyuk, J. M. Soures, C. Stoeckl, B. Yaakobi, and J. D. Zuegel, Nucl. Fusion **45**, S283 (2005).

2. P. W. McKenty, V. N. Goncharov, R. P. J. Town, S. Skupsky, R. Betti, and R. L. McCrory, Phys. Plasmas **8**, 2315 (2001); P. W. McKenty, T. C. Sangster, M. Alexander, R. Betti, R. S. Craxton, J. A. Delettrez, L. Elasky, R. Epstein, A. Frank, V. Yu. Glebov, V. N. Goncharov, D. R. Harding, S. Jin, J. P. Knauer, R. L. Keck, S. J. Loucks, L. D. Lund, R. L. McCrory, F. J. Marshall, D. D. Meyerhofer, S. P. Regan, P. B. Radha, S. Roberts, W. Seka, S. Skupsky, V. A. Smalyuk, J. M. Soures, K. A. Thorp, M. Wozniak, J. A. Frenje, C. K. Li, R. D. Petrasso, F. H. Séguin, K. A. Fletcher, S. Padalino, C. Freeman, N. Izumi, J. A. Koch, R. A. Lerche, M. J. Moran, T. W. Phillips, G. J. Schmid, and C. Sorce, Phys. Plasmas **11**, 2790 (2004).

3. M. C. Herrmann, M. Tabak, and J. D. Lindl, Phys. Plasmas **8**, 2296 (2001); R. Betti, K. Anderson, V. N. Goncharov, R. L. McCrory, D. D. Meyerhofer, S. Skupsky, and R. P. J. Town, Phys. Plasmas **9**, 2277 (2002).

4. L. Spitzer, Jr. and R. Härm, Phys. Rev. **89**, 977 (1953).

5. J. Delettrez, R. Epstein, M. C. Richardson, P. A. Jaanimagi, and B. L. Henke, Phys. Rev. A **36**, 3926 (1987); J. Delettrez, Can. J. Phys. **64**, 932 (1986).

6. R. C. Malone, R. L. McCrory, and R. L. Morse, Phys. Rev. Lett. **34**, 721 (1975).

7. S. P. Regan, R. Epstein, V. N. Goncharov, I. V. Igumenshchev, D. Li, P. B. Radha, H. Sawada, W. Seka, T. R. Boehly, J. A. Delettrez, O. V. Gotchev, J. P. Knauer, J. A. Marozas, F. J. Marshall, R. L. McCrory, P. W. McKenty, D. D. Meyerhofer, T. C. Sangster, D. Shvarts, S. Skupsky, V. A. Smalyuk, B. Yaakobi, and R. C. Mancini, Phys. Plasmas **14**, 056305 (2007).

8. T. R. Boehly, D. L. Brown, R. S. Craxton, R. L. Keck, J. P. Knauer, J. H. Kelly, T. J. Kessler, S. A. Kumpan, S. J. Loucks, S. A. Letzring, F. J. Marshall, R. L. McCrory, S. F. B. Morse, W. Seka, J. M. Soures, and C. P. Verdon, Opt. Commun. **133**, 495 (1997).

9. O. Gotchev, V. N. Goncharov, J. P. Knauer, T. R. Boehly, T. J. B. Collins, R. Epstein, P. A. Jaanimagi, and D. D. Meyerhofer, Phys. Rev. Lett. **96**, 115005 (2006).

10. V. N. Goncharov, O. V. Gotchev, E. Vianello, T. R. Boehly, J. P. Knauer, P. W. McKenty, P. B. Radha, S. P. Regan, T. C. Sangster, S. Skupsky, V. A. Smalyuk, R. Betti, R. L. McCrory, D. D. Meyerhofer, and C. Cherfils-Clérouin, Phys. Plasmas **13**, 012702 (2006).

11. W. L. Kruer, *The Physics of Laser–Plasma Interactions*, Frontiers in Physics, Vol. 73, edited by D. Pines (Addison-Wesley, Redwood City, CA, 1988).

12. B. Yaakobi, C. Stoeckl, T. Boehly, D. D. Meyerhofer, and W. Seka, Phys. Plasmas **7**, 3714 (2000); B. Yaakobi, T. R. Boehly, T. C. Sangster, D. D. Meyerhofer, B. A. Remington, P. G. Allen, S. M. Pollaine, H. E. Lorenzana, K. T. Lorenz, and J. A. Hawreliak, Phys. Plasmas **15**, 062703 (2008).

13. National Research Council (U.S.) Committee on High Energy Density Plasma Physics, *Frontiers in High Energy Density Physics: The X-Games of Contemporary Science* (National Academies Press, Washington, DC, 2003), p. 84.

14. S. Ichimaru, Rev. Mod. Phys. **54**, 1017 (1982).

15. A. Ng *et al.*, Laser Part. Beams **23**, 527 (2005).

16. S. H. Glenzer *et al.*, Phys. Plasmas **6**, 2117 (1999).

17. O. L. Landen *et al.*, J. Quant. Spectrosc. Radiat. Transf. **71**, 465 (2001).

18. S. H. Glenzer *et al.*, Phys. Rev. Lett. **90**, 175002 (2003).

19. T. R. Boehly, J. A. Delettrez, J. P. Knauer, D. D. Meyerhofer, B. Yaakobi, R. P. J. Town, and D. Hoarty, Phys. Rev. Lett. **87**, 145003 (2001).

20. D. J. Hoarty *et al.*, J. Quant. Spectrosc. Radiat. Transf. **99**, 283 (2006).

21. S. H. Glenzer *et al.*, Phys. Rev. Lett. **98**, 065002 (2007).

22. H. Sawada, S. P. Regan, D. D. Meyerhofer, I. V. Igumenshchev, V. N. Goncharov, T. R. Boehly, R. Epstein, T. C. Sangster, V. A. Smalyuk, B. Yaakobi, G. Gregori, S. H. Glenzer, and O. L. Landen, Phys. Plasmas **14**, 122703 (2007).

23. Prism Computational Sciences, Inc., Madison, WI 53711.

24. S. P. Regan, H. Sawada, V. N. Goncharov, D. Li, P. B. Radha, R. Epstein, J. A. Delettrez, S. X. Hu, V. A. Smalyuk, B. Yaakobi, T. C. Sangster, D. D. Meyerhofer, R. L. McCrory, and R. C. Mancini, "Spectroscopic Observations of Fermi-Degenerate Aluminum Compressed and Heated to Four Times Solid Density and 20 eV," submitted to Physical Review Letters.

25. J. J. MacFarlane *et al.*, High Energy Density Phys. **3**, 181 (2006).

26. T. J. Kessler, Y. Lin, J. J. Armstrong, and B. Velazquez, in *Laser Coherence Control: Technology and Applications*, edited by H. T. Powell and T. J. Kessler (SPIE, Bellingham, WA, 1993), Vol. 1870, pp. 95–104.

27. S. Skupsky, R. W. Short, T. Kessler, R. S. Craxton, S. Letzring, and J. M. Soures, J. Appl. Phys. **66**, 3456 (1989).

28. T. R. Boehly, V. A. Smalyuk, D. D. Meyerhofer, J. P. Knauer, D. K. Bradley, R. S. Craxton, M. J. Guardalben, S. Skupsky, and T. J. Kessler, J. Appl. Phys. **85**, 3444 (1999).

29. J. P. Knauer, R. Betti, D. K. Bradley, T. R. Boehly, T. J. B. Collins, V. N. Goncharov, P. W. McKenty, D. D. Meyerhofer, V. A. Smalyuk, C. P. Verdon, S. G. Glendinning, D. H. Kalantar, and R. G. Watt, Phys. Plasmas **7**, 338 (2000).

30. D. H. Kalantar *et al.*, in *22nd International Congress on High-Speed Photography and Photonics*, edited by D. L. Paisley and A. M. Frank (SPIE, Bellingham, WA, 1997), Vol. 2869, pp. 680–685.

31. B. L. Henke, E. M. Gullikson, and J. C. Davis, At. Data Nucl. Data Tables **54**, 181 (1993).

32. B. L. Henke, J. P. Knauer, and K. Premaratne, J. Appl. Phys. **52**, 1509 (1981).

33. H. Sawada, "Experimental Investigation of a Direct-Drive Shock Wave Heated and Compressed Planar Target Relevant to ICF," Ph.D. thesis, University of Rochester, 2008.

34. S. P. Regan, Laboratory for Laser Energetics, private communication (2008).

35. D. K. Bradley, P. M. Bell, J. D. Kilkenny, R. Hanks, O. Landen, P. A. Jaanimagi, P. W. McKenty, and C. P. Verdon, Rev. Sci. Instrum. **63**, 4813 (1992).

36. V. N. Goncharov, T. C. Sangster, P. B. Radha, R. Betti, T. R. Boehly, T. J. B. Collins, R. S. Craxton, J. A. Delettrez, R. Epstein, V. Yu. Glebov, S. X. Hu, I. V. Igumenshchev, J. P. Knauer, S. J. Loucks, J. A. Marozas, F. J. Marshall, R. L. McCrory, P. W. McKenty, D. D. Meyerhofer, S. P. Regan, W. Seka, S. Skupsky, V. A. Smalyuk, J. M. Soures, C. Stoeckl, D. Shvarts, J. A. Frenje, R. D. Petrasso, C. K. Li, F. Séguin, W. Manheimer, and D. G. Colombant, Phys. Plasmas **15**, 056310 (2008).

37. W. F. Huebner *et al.*, Los Alamos National Laboratory, Los Alamos, NM, Report LA-6760-M (1977).

38. S. P. Lyon and J. D. Johnson, Los Alamos National Laboratory, Los Alamos, NM, Report LA-UR-92-3407 (1992).

39. R. C. Mancini *et al.*, Comput. Phys. Commun. **63**, 314 (1991).

40. C. A. Iglesias, J. L. Lebowitz, and D. MacGowan, Phys. Rev. A **28**, 1667 (1983).

41. D. A. Haynes, Jr., D. T. Garber, C. F. Hooper, Jr., R. C. Mancini, Y. T. Lee, D. K. Bradley, J. Delettrez, R. Epstein, and P. A. Jaanimagi, Phys. Rev. E **53**, 1042 (1996).

42. B. L. Henke, E. M. Gullikson, and J. C. Davis, At. Data Nucl. Data Tables **54**, 181 (1993).

43. P. A. Jaanimagi, Laboratory for Laser Energetics, private communication (2008).

44. C. I. Szabó, *et al.*, Radiat. Phys. Chem. **75**, 1824 (2006).

45. P. R. Bevington, *Data Reduction and Error Analysis for the Physical Sciences* (McGraw-Hill, New York, 1969), p. 53.

46. A. Sunahara, J. A. Delettrez, C. Stoeckl, R. W. Short, and S. Skupsky, Phys. Rev. Lett. **91**, 095003 (2003).

47. S. E. Bodner, J. Fusion Energy **1**, 221 (1981).

48. A. Simon, R. W. Short, E. A. Williams, and T. Dewandre, Phys. Fluids **26**, 3107 (1983).

49. C. Stoeckl, R. E. Bahr, B. Yaakobi, W. Seka, S. P. Regan, R. S. Craxton, J. A. Delettrez, R. W. Short, J. Myatt, A. V. Maximov, and H. Baldis, Phys. Rev. Lett. **90**, 235002 (2003).

50. S. P. Regan, J. A. Marozas, J. H. Kelly, T. R. Boehly, W. R. Donaldson, P. A. Jaanimagi, R. L. Keck, T. J. Kessler, D. D. Meyerhofer, W. Seka, S. Skupsky, and V. A. Smalyuk, J. Opt. Soc. Am. B **17**, 1483 (2000).

51. P. B. Radha, V. N. Goncharov, T. J. B. Collins, J. A. Delettrez, Y. Elbaz, V. Yu. Glebov, R. L. Keck, D. E. Keller, J. P. Knauer, J. A. Marozas, F. J. Marshall, P. W. McKenty, D. D. Meyerhofer, S. P. Regan, T. C. Sangster, D. Shvarts, S. Skupsky, Y. Srebro, R. P. J. Town, and C. Stoeckl, Phys. Plasmas **12**, 032702 (2005).